The Simultaneous Measurement of Reversed Phase-Encoding EPI in a Single fMRI Session at 7T: Quantitative and Qualitative Evaluation of Geometric Distortion Correction in Submillimetre fMRI

Seong Dae Yun[1*], Erhan Genc[2], N. Jon Shah[1,3,4,5]

[1]Institute of Neuroscience and Medicine 4, INM-4, Forschungszentrum Jülich, Jülich, Germany

[2]Department of Psychology and Neurosciences, Leibniz Research Centre for Working Environment and Human Factors (IfADo), Dortmund, Germany

[3]Institute of Neuroscience and Medicine 11, INM-11, JARA, Forschungszentrum Jülich, Jülich, Germany

[4]JARA - BRAIN - Translational Medicine, Aachen, Germany

[5]Department of Neurology, RWTH Aachen University, Aachen, Germany

*** Correspondence:**
Dr. Seong Dae Yun (s.yun@fz-juelich.de)

Institute of Neuroscience and Medicine (INM-4), Forschungszentrum Jülich, Leo-Brandt-Strasse, 52425 Jülich, Germany

Running title: Simultaneous Acquisition of Reversed-PE EPI

Keywords: Co-registration, Distortion correction, EPI, fMRI, Functional mapping accuracy, Reversed phase-encoding, Submillimetre, and Ultra-high field. (Min.5-Max. 8)

Article type: Original Research (5020 words; 2 Tables and 6 Figures)

The manuscript has been written in British English.

Abstract

Motivation: Currently, geometric distortions in EPI are generally corrected using a method that employs the reversed phase-encoding direction. This approach is usually implemented by applying an extra run of the same protocol, only with the phase-encoding direction changed, leading to a substantial increase in redundant acquisition time and specific absorption ratio. Furthermore, while the distortion correction method has been widely employed in numerous fMRI studies, its impact on submillimetre fMRI analysis has remained largely unexplored.

Methods: This work presents an EPI scheme that acquires both the original and reversed phase-encoding data in a single fMRI session. The feasibility of using the method for submillimetre EPI (0.73×0.73 mm^2) was verified with visual fMRI at 7T. EPI distortions were corrected using the ANTs software, and its performance was evaluated using various criteria, including spatial resolution, functional mapping accuracy, and histogram distribution.

Results: The presented scheme effectively reduced redundant acquisition time and therefore total radio-frequency energy. The distortion-corrected fMRI data demonstrated significant improvements in co-registration with anatomical scans and functional mapping accuracy. As a result, the ratio of grey-matter-activated voxels was substantially enhanced (on average, 88.58%). These improvements were achieved without significant degradation of spatial resolution or alternation of the functional activation distribution; a high degree of similarity between the original and distortion-corrected cases ($\rho > 0.99$) was observed in the t-value histograms.

Conclusions: This work presents a simultaneous acquisition scheme for reversed phase-encoding EPI, demonstrating its effectiveness and the benefits achieved through distortion correction in submillimetre fMRI at 7T.

1. Introduction

Echo planar imaging (EPI) can significantly shorten acquisition times by acquiring multiple phase-encoding (PE) lines per excitation pulse. The relatively high temporal resolution of EPI is particularly well-suited for detecting time-dependent variation in signal contrasts, resulting in its widespread use in dynamic MR applications, such as diffusion MRI, perfusion MRI and functional MRI (fMRI). Since the advent of EPI (Mansfield, 1977), its performance has been substantially enhanced by virtue of the development of hardware and imaging techniques, which enables the robust utilisation of high-resolution EPI in both clinical and research applications.

However, the relatively long acquisition window of EPI along the PE direction contributes to the development of more phase errors in this direction, resulting in substantial geometric deformation of tissue structures. Although this geometric distortion can be effectively mitigated through improved shimming (Balteau et al., 2010; Kim et al., 2016) or readout-acceleration techniques, such as parallel imaging (Griswold et al., 2002), partial Fourier (Margosian 1985), or multi-shot approaches, they may necessitate technically more demanding configurations, especially when operating at higher field strengths or aiming for higher resolution imaging with an increased readout length.

Therefore, a more attractive solution is the direct unwarping of geometric distortions in the post-data processing stage. Various approaches have been attempted for this purpose, including B_0-field maps (Chen and Wyrwicz, 1999; Jezzard and Balaban, 1995; Hutton et al., 2002), point-spread-function (PSF) (Chung et al., 2011; Patzig et al., 2020; Robson et al., 1997; Zaitsev et al., 2004; Zeng and Constable 2002), deep learning (Duong et al., 2020), or reversed PE methods (Chang and Fitzpatrick, 1992; Morgan et al., 2004). Here, both the B_0-field map and PSF methods require another dedicated imaging sequence, which may not be available on site. Moreover, the noise sensitivity of phase unwrapping or the intentional smoothing in the B_0-field map method can yield inaccurate distortion-correction (Holland et al., 2010; Hong et al., 2015; Hutton et al., 2002; Renvall et al., 2016). While the PSF approach outperforms the B_0-field map method in terms of robustness to noise, potentially making it more accurate (Patzig et al., 2020), the PSF measurements require a relatively long acquisition time (Holland et al., 2010), which becomes longer as the imaging matrix size grows for high spatial resolution. For real-time distortion correction, a deep learning-based technique has also been developed, albeit with the requirement of an excessively long training time and the potential need to resize

the input data to match the dimensions of the trained data sets. Due to the difficulties described above, one widely used method in the community is to utilise the reversed PE direction. This approach exploits the fact that the distortions in the reversed PE data also develop toward the opposite direction, enabling the data-driven calculation and relocation of voxel shifts between the two different PE directions without prior knowledge of the B_0 offset or PSF. Furthermore, the reversed PE data can be obtained using the same sequence, indicating that no additional sequence implementation is required.

However, the reversed-PE method is typically implemented by adding an extra run of the same EPI protocol, only with the change of the PE direction, leading to a substantial increase in redundant acquisition time and specific absorption ratio (SAR) for parallel imaging calibration scan. Therefore, this work aims to present a novel EPI scheme that additionally measures EPI data with the reversed PE direction within a single fMRI session. This scheme is expected to reduce total acquisition time, particularly for fMRI with a large imaging matrix size aimed at high spatial resolution and whole-brain coverage. In addition, despite the fact that the use of reversed PE method has been demonstrated in numerous previous submillimetre fMRI studies (Huang et al., 2021; Kashyap et al., 2017; Marquardt et al., 2018; Navarro et al., 2021; Jia et al., 2020; Schellekens et al., 2023; Yun et al., 2023a), most of them preclude an analysis of the performance of distortion-correction and its potential impact on high-resolution fMRI data. The results presented in literature (Duong et al., 2020; Dymerska et al., 2018; Hutton et al., 2002; Montez et al., 2023; Patzig et al., 2020) have mainly focused on improvements in the geometric structure of distortion-corrected EPI and the corresponding co-registration accuracy between it and the anatomical scan. Moreover, the EPI data employed in these studies are often limited to a spatial resolution at the millimetre scale (i.e. > 1 mm), leaving the impact of the distortion correction on submillimetre fMRI largely unexplored. Hence, another aim of the present work is to perform quantitative and qualitative evaluation of geometric distortion-correction in submillimetre (0.73×0.73 mm^2) fMRI at 7T and assess its effects on the spatial resolution, functional mapping accuracy, and distribution of activated voxels.

2. Materials and Methods

2.1. Study subject and ethics statement

All *in vivo* measurements were performed on healthy volunteers who underwent standard safety screening procedures. None of them had any medical conditions or suffered from any neurological or psychiatric illnesses. After providing a complete study description, written informed consent was obtained prior to scanning. The local institutional review board (RWTH Aachen University, Germany) approved the study protocol (EK 346/17), screening questionnaires, and consent forms (Yun et al., 2022). Five healthy volunteers (four males, one female; mean age, 28.4 years; range, 21-39 years) were recruited for the present study. For each subject, a visual fMRI run using the proposed EPI scheme and with an additional MP2RAGE acquisition was performed.

2.2. Proposed EPI scheme

Figure 1a shows a schematic representation of a typical fMRI run using the standard EPI scheme, consisting of three stages: calibration, dummy, and actual fMRI scans. Before starting the actual fMRI scans, two preceding measurements, namely calibration and dummy scans, are performed, which are necessary for the reconstruction of acceleration techniques and for reaching a steady state (Yun et al., 2023b). The acquisition of calibration data is assumed to be included here, as most high-resolution fMRI protocols commonly employ acceleration techniques. In the standard scheme, the fMRI scans are only acquired with a single PE direction, as indicated with the blue arrows in the 1st row of Fig. 1a. Here, EPI with the reversed PE is performed by adding the second run of the same protocol, only changing the PE direction to the opposite direction; see the red arrows in the 2nd row of Fig. 1a. This indicates that the second session still requires another complete acquisition of the calibration data, although the reversed-PE EPI data need to be acquired only for a few temporal volumes.

While the fMRI scan is acquired using EPI, the calibration scan for the parallel imaging is often acquired using a sequence more tolerant to field inhomogeneities, such as a conventional line-by-line excitation, spoiled gradient-recalled (SPGR) sequence. This approach ensures a more robust kernel calibration at ultra-high fields, where the effects of field inhomogeneities on EPI are expected to be more pronounced. However, the SPGR scheme requires a relatively long acquisition time, thereby making the repeated acquisition of the calibration scan in the standard scheme more redundant.

To avoid this conflict, the proposed scheme adjusts the EPI acquisition such that the first two EPI scans in the dummy stage are acquired with the reversed PE direction (Yun et al., 2023b), as depicted in Fig. 1b. The same calibration kernel can be used to reconstruct both the original and reversed-PE EPI data, subsequently leading to an effective reduction of total acquisition time and SAR for the parallel imaging calibration scan. For quantitative evaluation, the amount of this reduction was simulated using the Siemens sequence development platform, 'IDEA' (Integrated Development Environment for Applications), under the baseline version of N4_VE12U_LATEST_20181126. In this work, the number of dummy and reversed PE scans is set to four and two, respectively, as shown in the figure.

2.3. Imaging protocols: submillimetre fMRI

A visual checkerboard paradigm was employed for *in vivo* fMRI experiments to elicit circumscribed activation in the visual cortex (Yun et al., 2013, 2017). The passive viewing task involved a simple block design in which a black and white checkerboard, reversing at a frequency of 8 Hz, alternated with low-level baseline phases (fixation cross). The paradigm consisted of four dummy scans for reaching a steady state, followed by 96 scans comprising eight cycles of baseline-activation states. Each cycle lasted six volume acquisitions, resulting in a total duration of 21 seconds. As described in the previous section, the first two dummy scans were acquired with the reversed PE direction.

The feasibility of using the proposed EPI scheme for visual fMRI was verified with the following imaging parameters: TR/TE = 3500/22 ms, FOV (AP × LR × FH) = 210 × 210 × 117 mm^3, matrix = 288 × 288 with 117 axial slices (0.73 × 0.73 × 1.0 mm^3), flip angle = 90°, partial Fourier = 5/8, parallel imaging = 3-fold, multi-band = three-fold, and receiver bandwidth = 965 Hz/Px. The parallel imaging calibration data were acquired using the SPGR sequence with an auto-calibration signal (ACS) size of 72. A 3D anatomical image was acquired using a T_1-weighted magnetisation-prepared, rapid gradient echo (MP2RAGE) sequence with the following configuration: TR/TE/TI_1/TI_2 = 4440/2.08/840/2370 ms, FOV (FH × AP × LR) = 240 × 226 × 154 mm^3, matrix size = 400 × 376 with 256 sagittal slices (0.6 mm isotropic), flip angles = 5°/6°, parallel imaging = 3-fold, and receiver bandwidth = 250 Hz/Px. The above imaging setup was implemented on a Siemens Magnetom Terra 7T scanner with a single-channel Tx and 32-channel Rx Nova medical coil supplied by the manufacturer.

2.4. Distortion correction: qualitative and quantitative evaluation

The first two EPI images acquired with the reversed PE were utilised in the distortion correction of the original fMRI time-series data (i.e. 96 temporal volumes). To accomplish this, an open medical image processing toolkit, Advanced Normalization Tools (ANTs) (https://github.com/srikash; https://github.com/ANTsX/ANTs; Avants et al., 2010; Esteban et al., 2019; Tustison et al., 2021), was employed in this work. This software calculates the warping field of the original EPI data while estimating subject motion displacements, enabling simultaneous correction of both motion and distortion through the time-series in a single interpolation step. This strategy is beneficial for minimising potential degradation of spatial resolution that could occur during the data preprocessing step (Glasser et al., 2013; Wang et al., 2022).

It has been previously reported that the distortion correction step involves resampling of voxels or sub-voxel shifts, which can result in a loss of effective spatial resolution (Hutton et al., 2002; Kashyap et al., 2018; Polimeni et el., 2018; Renvall et al., 2016; Wang et al., 2022). In the present work, the degree of spatial resolution degradation due to the unwarping process in the distortion correction is thoroughly investigated using an approach similar to that suggested in previous work (Renvall et al., 2016). Here, the original EPI image underwent the standard spatial smoothing step provided by SPM12 (Wellcome Department of Imaging Neuroscience, UCL, London, UK; https://www.fil.ion.ucl.ac.uk/spm/software/spm12/) for a range of Gaussian smoothing kernel widths (i.e. 0.15, 0.2 and 0.3 mm). A region-of-interest (ROI) was selected in the white matter (WM), where the signal variation in the region was relatively homogeneous, and the standard deviation (SD) within the ROI was computed for the original as well as the smoothed EPI images. The results were then compared to that of the distortion-corrected EPI image.

The original and distortion-corrected EPI images were individually co-registered to the MP2RAGE scan using the ‘antsRegistrationSyN’ processing module in the ANTs toolkit. In each case, the co-registration accuracy was assessed by comparing the structural differences between the EPI and the MP2RAGE scans. For illustrative purposes, the background noise of the MP2RAGE scan, generated from combining the two inversion images into a single unified image, was removed using a dedicated script (https://github.com/JosePMarques/MP2RAGE-related-scripts).

For the original and distortion-corrected fMRI data sets, the first-level analysis was separately performed using the generalised linear model in SPM12, and the functional results obtained (uncorrected p-value < 0.001) were overlaid on their respectively co-registered

MP2RAGE scan. Putative differences in the localisation of the activated voxels in the grey matter (GM) were quantitatively examined by calculating the ratio of activated voxels located in the GM to those in other regions (i.e. non-GM). For this analysis, only the activated voxels with t-values equal to or greater than five were selected to reduce the number of false positives in the calculation (Lohmann et al., 2018). Lastly, the impact of the distortion correction on the functional activation was inspected by analysing the histogram distribution of the activated voxels. The histogram results obtained from the original and distortion-corrected fMRI data were compared, and the degree of matching between the two cases was quantitatively measured by computing the Pearson correlation coefficient.

3. Results

3.1. Distortion correction using the proposed scheme

Figure 2 shows the results of distortion correction from a single-volume functional scan at four representative slice locations, with the first and second rows displaying images obtained from the reversed (1st scan) and original PE (5th scan) directions. The last row shows the corresponding distortion-corrected results, revealing no significant visible loss of spatial resolution at any of the displaced slice locations. This result also demonstrates that the proposed simultaneous acquisition scheme for reversed PE EPI can be feasibly used in the distortion correction. The distortion-corrected results at entire slice locations can be found in Supplementary File (see Supplementary Figure 1).

Table 1 shows the acquisition time and SAR required for the parallel imaging calibration scan when acquired using the SPGR sequence and compares them with those needed for the entire fMRI acquisition. The results were obtained for a range of ACS lines (i.e. 24, 48, and 72) and TRs (i.e. 10, 15, and 20 ms) of the SPGR sequence. It is important to note that the SAR values shown in the table represent the time-averaged radio frequency (RF) power (i.e. W), calculated at a commonly used flip angle of 15°. The table reveals that the required acquisition time increases with higher numbers of ACS lines or longer TR values. While the ACS acquisition time constituted a relatively small portion compared to the total acquisition time, it reached as high as 192 s, when acquired with a TR of 20 ms and 72 ACS lines. The implications of using a relatively long TR and a large number of ACS lines will be discussed later. Furthermore, the table demonstrates that SAR decreases for longer TR values, as readily expected. However, SAR also decreases for a greater number of ACS lines. This is due to the fact that the RF energy per unit time dissipated in the parallel imaging calibration scan is much smaller than that of the main fMRI scan, as it is implemented with large flip angles for the main excitation (90°) and the fat-saturation module (110°). Conversely, when the calibration data are acquired with a relatively short TR and small ACS lines (i.e. 10 ms with 24 ACS lines), SAR accounts for as much as 46% of the total SAR required. The above results suggest that the proposed simultaneous acquisition scheme can significantly reduce the redundant SAR and acquisition time for the acquisition of reversed PE EPI.

3.2. Assessment of spatial resolution

Figure 3a displays the original EPI images at four selected slice locations where the quantitative assessment of spatial resolution was performed. For each slice, the ROI in which the SD of the signal variations was computed is delineated in yellow, and the results are shown in Fib. 3b with respect to the smoothing kernel width. For all of the above slices, a decrease in SD can be observed as the smoothing kernel width increases, meaning that the spatial resolution is degrading. In comparison to that, the SD of the distortion-corrected EPI was shown to be larger than that of the original image smoothed with a kernel width of 0.20 mm as all slice locations; the result at the 2nd and 4th slice locations exhibited even higher SD than the case of kernel width of 0.15 mm.

For visual inspection of the spatial resolution, another ROI was selected for each slice (marked in green). Its enlarged representation is shown in Fig. 3b, where the degradation of spatial resolution is visually apparent as the kernel width increases. The corresponding distortion-corrected images exhibit features very comparable to the original image smoothed at a kernel width of around 0.15 mm. The above quantitative and qualitative assessment results indicate that the loss of spatial resolution induced by the distortion correction was not significant.

3.3. Co-registration between the functional and anatomical scan

The EPI images, co-registered with the MP2RAGE scan, were transformed from the subject space to the anatomical space, and results from a representative subject are shown in Fig. 4. Both the EPI and MP2RAGE scans are presented in three sectional views (i.e. axial, coronal and sagittal), each depicting the counterpart of the brain. That is, for the axial and coronal presentation, the EPI and MP2RAGE scans display the left and right hemispheres, whereas, for the sagittal presentation, they show the upper and lower halves, respectively.

To aid visual comparison, the contour of the ventricles (i.e. the lateral and fourth ventricles) obtained from the MP2RAGE scan are depicted in yellow. Here, improved alignments between the EPI and MP2RAGE scans are clearly observed in the distortion-corrected case (Fig. 4b) when compared to the original, uncorrected one (Fig. 4a); a substantial misalignment of the ventricles in the boundaries between the two scans can be found in the original EPI case. For illustrative purposes, the aforementioned ventricle areas are extracted from the EPI images using signal thresholding, and the results from both the original EPI (red-yellow) and corrected EPI (blue-light blue) images are overlaid onto the MP2RAGE scan in Fig. 4c. This clearly illustrates the substantial improvements in co-registration achieved

through distortion-correction. Specifically, in the sagittal presentation, the geometric deformations present in the frontal lobe of the original EPI image (i.e. shrunken structures) are demonstrated to be effectively reduced in the distortion-corrected case. As a result, the boundary between the cingulate gyrus and corpus callosum is also well aligned between the EPI and MP2RAGE scans, as indicated by the regions marked by red arrows.

3.4. Analysis of fMRI data

Figure 5 shows activated voxels obtained from the original (red-white) and distortion-corrected (cyan-magenta) fMRI data sets, each of which is overlaid on the respective co-registered MP2RAGE scan. Substantial differences in the distribution of activated voxels are clearly observable in the depiction of both original and distortion-corrected results on the same MP2RAGE scan (Fig. 5a). In order to examine the localisation of the activated voxels within the cortical ribbon, the GM contour was extracted from the MP2RAGE scan, and is displayed in a separate representation of the original and distortion-corrected results (Figures 5b and c).

It is observed that the activated voxels in the distortion-corrected case are more accurately localised within the cortical ribbon. In the original, uncorrected case, a significant number of activated voxels are identified outside the GM region, as is clearly seen in the enlarged representation of the selected rectangular ROIs in Figures 5b and c. Table 2 shows the ratio of activated voxels located in the GM and non-GM regions. The ratio of the GM-located activated voxels was substantially increased in the distortion-corrected case when compared to the original one. This was consistently observed for all five subjects. The mean ± SD ratio of the GM-located activated voxels in the distortion-corrected case was 88.58 ± 2.51%, which was, on average, 8.33% greater than that of the original one, i.e. 80.25 ± 1.69%. This result quantitatively verifies the improvement in the localisation of the activated voxels within the GM achieved through distortion correction.

Figure 6 shows the histogram distribution of t-values obtained from the original and distortion-corrected fMRI data sets, with each represented in blue and orange on the same plot. The results are displayed for all five subjects, along with the computed Pearson correlation coefficients between the two histograms. Visual inspection of the histogram distribution suggests that the results from the original and distortion-corrected cases exhibit very similar features, implying that the distortion correction did not have any significant impact on the distribution of functional activation. The high degree of similarity in the histogram distribution

was further confirmed by the computed correlation coefficients, all of which exceeded 0.99 for all subjects.

4. Discussion

This work introduces an EPI scheme that acquires both original and reversed PE-direction data in a single time-series session and demonstrates its applicability for submillimetre fMRI at 7T. The proposed scheme effectively reduces the need for additional acquisition time and RF energy accumulation, as required by the standard EPI scheme when acquiring reversed PE data. This advantage becomes more prominent when the parallel imaging calibration scan is acquired using the SPGR sequence for a more robust calibration of the reconstruction kernel, particularly at ultra-high fields. The current study also employed the SPGR sequence, configured with 72 ACS lines. The selection of this relatively large number aimed to improve the quality of reconstructed images, as many ACS lines effectively mitigate aliasing artefacts or noise by comprehensively capturing low-frequency signals (Chang et al., 2022; Sheng et al., 2021). Although this benefit comes at the cost of longer acquisition times, the use of a greater number of ACS lines serves as a straightforward solution for enhanced image reconstruction unless more elaborated sampling methods (Park et al., 2005; Wang et al., 2022) or advanced kernel calibration techniques (Aja-Fernández et al., 2015; Chang et al., 2022; Sheng et al., 2021) are implemented.

Based on the sequence configuration tested here, the use of a larger number of ACS lines was also demonstrated to reduce the time-averaged RF power. This was mainly attributed to the lower RF energy dissipation per unit time during the parallel imaging calibration compared to the main fMRI scan. At ultra-high fields, the increased demand in SAR often exceeds the permitted level, thereby hindering the steady operation of the sequence. Therefore, the increased number of ACS lines or, more obviously, the longer TR in the parallel imaging calibration scan can effectively alleviate the SAR issue, while the other primary fMRI parameters are maintained unchanged. Nonetheless, this approach significantly increases the scanning time for acquiring parallel imaging calibration data, which in turn prolongs the acquisition time for reversed PE EPI data to the same extent in the standard EPI scheme. In contrast, the simultaneous scheme presented in this work eliminates the need for redundant acquisition of the parallel imaging calibration scan for reversed PE EPI, resulting in substantial time savings for the overall acquisition. However, it is worth noting that even in cases with a relatively small number of ACS lines or a short TR (e.g. 24 lines and 10 ms), the proposed scheme has also been proven effective in minimising unnecessary RF power accumulation.

In addition to the aforementioned benefits, the direct acquisition of the reversed PE EPI in a single measurement can greatly simplify an fMRI protocol set, particularly in cases where multiple fMRI sessions are involved. This approach also helps to avoid the risk of inadvertently missing the acquisition of reversed PE data, which may occur in the standard scheme due to the need for a separate measurement for each fMRI session. Moreover, the proposed scheme opens the possibility of a more direct distortion correction of fMRI data through online reconstruction platforms such as the ICE- Gadgetron (https://github.com/gadgetron/gadgetron), making it suitable for straightforward use in clinical diagnosis (Yun et al., 2023b). Additionally, the simultaneous scheme minimises potential differences in subject motion between the acquisition of original and reversed PE EPI, reducing the motion blur during the registration of the two different PE data sets in distortion correction (Holland et al., 2010).

One frequently addressed concern associated with distortion correction is the potential loss of spatial resolution arising from the unwarping process, that involves resampling or repositioning of voxels (Hutton et al., 2002; Kashyap et al., 2018; Renvall et al., 2016). Despite the widespread use of the reversed PE method in many high-resolution fMRI studies, its impact on spatial resolution has not been extensively explored. In this work, this issue was quantitatively and qualitatively assessed in the context of submillimetre fMRI, utilising the ANTs software package for distortion correction. The results obtained demonstrate that the loss of spatial resolution observed in our distortion-corrected images was minimal. In the community, other various software packages are also available for distortion correction (Yun et al., 2023b), including 3DQwarp (AFNI)(https://afni.nimh.nih.gov/pub/dist/doc/program_help/3dQwarp.html), COPE (Brain Voyager)(https://support.brainvoyager.com/brainvoyager/available-tools/86-available-plugins/62-epi-distortion-correction-cope-plugin), and TOPUP (FSL)(https://fsl.fmrib.ox.ac.uk/fsl/fslwiki/topup), all of which have been employed in numerous previous submillimetre fMRI studies. In future work, the performance of these alternative distortion-correction software will be assessed in comparison to the ANTs, with the aim of determining the most optimal method for high-resolution fMRI.

Submillimetre fMRI enables the detection of neural signals with cortical depth dependence, which facilitates the investigation of the fundamental processing of brain functions and their linked pathways between intra-cortical tissues (Yun et al., 2023). For this purpose, the cortical layers or columns need to be determined, typically using the structural

information derived from the anatomical scan (Deshpande et al., 2022; Jia et al., 2021; Margalit et al., 2020). Thus, precise co-registration between the functional and anatomical scans is a crucial factor for the successful delineation of the cortical depth-dependent functional profiles. The distortion correction demonstrated here exhibited significant improvements in the co-registration between the EPI and MP2RAGE scans, which is expected to benefit the definition of the cortical depths. However, the distortion-corrected EPI images still suffer from the susceptibility-induced signal loss, which can be seen in regions around the frontal lobe. This can be further reduced by employing dedicated RF pulses, also known as tailored RF methods (Yip et al., 2006 and Zheng et al., 2013), or utilising an EPI-readout shortening technique such as EPI with Keyhole (EPIK)(Shah and Zilles, 2003, 2004; Zaitsev et al., 2001), the use of which has been demonstrated in a number of fMRI studies (Yun et al., 2013, 2019; Yun and Shah, 2017) including those focused on delineating the cortical depth-dependent profiles (Pais-Roldán et al., 2023; Yun et al., 2022). In this study, the target functional area was the visual cortex, where the susceptibility-induced signal loss is expected to be minimal. This allowed the investigation of the effect of distortion correction on functional activation with little concern for the signal loss issue.

The improved co-registration from the distortion-corrected data directly contributed to enhancing the accuracy of functional mapping onto the GM. Here, the distortion correction did not significantly affect the distribution of functional activation. In the distortion-corrected case, the ratio of GM-located activated voxels was substantially higher when compared to the original, uncorrected one. Nevertheless, a fraction of the activated voxels still appeared in the non-GM regions, with an average ratio of 11.42% across the five-subject data sets. Several possible reasons exist for the presence of non-GM activated voxels. One explanation is imperfect distortion correction and the subsequent errors in co-registration. Another reason can be the false positive activation induced from motion or physiological fluctuations such as respiration or cardiac pulse (Birn et al., 2006; Bright et al., 2013). However, the impact of physiological noise can be controlled to some extent by simultaneously recording the physiological signals during fMRI and regressing them out from the fMRI time-series data (Birn et al., 2006). Another potential reason is the superficial bias effect typically seen in the gradient-echo BOLD methods. For the reduction of this effect, various attempts have been proposed, including the use of prior information on venous structures (Kay et al., 2019; Koopmans et al., 2010) or phase-data-based regression methods (Menon et al., 2002; Stanley et al., 2021). Therefore, when our fMRI setting is further combined with the physiological-

noise or the superficial-bias control methods, an even greater ratio of GM-located activated voxels is expected.

A distortion-matched anatomical scan, the readout of which is performed using the same EPI sequence as for fMRI, can be used as an alternative to the distortion correction method (Chai et al., 2021; van der Zwaag et al., 2018). Accordingly, the anatomical scan exhibits identical distortions to the fMRI scan, ensuring errorless co-registration between the two scans. This approach makes the co-registration process more straightforward compared to the scenario involving two different sequence modalities (e.g. EPI and MP2RAGE) (Kashyap et al., 2018; Navarro et al., 2021). However, due to the distorted anatomical reference, its application can be limited for the analyses that rely on accurate anatomical information, such as the morphometric measurement of cortical thickness or the cortical surface-based atlasing (Polimeni et al., 2018, Yun et al., 2023a). The distortion in this anatomical scan can also be corrected using the reversed PE method. In this case, the same simultaneous acquisition scheme proposed in this work can be effectively deployed to minimise the total acquisition time and energy accumulation.

One limitation of the reversed PE method is its relatively time-consuming process. In our fMRI data, which consists of 96 temporal volumes, each containing 9.7 M voxels (i.e. 288 × 288 × 117 slices), the processing time on a standalone PC (Intel Core i7-8850H CPU 2.60 GHz with 32GB RAM) was approximately 6.5 hours. The processor used here has a single socket and 12 parallel processing threads, which were fully exploited during the ANTs computation. However, given that our processor is relatively old (Intel Core 8th generation, released in Apr. 2018), the use of a more powerful processor with multiple sockets under a workstation environment (e.g. eight sockets, 48 threads with Intel Xeon Processor E7, yielding 384 parallel processing threads), could drastically reduce the processing time, allowing for a timely reconstruction for entire submillimetre fMRI data with distortion correction.

In conclusion, this work presents an alternative EPI scheme that simultaneously acquires reversed PE data in a single measurement, and its utility for submillimetre (0.73 × 0.73 mm^2) fMRI has been demonstrated at 7T. This strategy effectively spares another acquisition time and RF energy accumulation for the parallel imaging calibration scans, making the method particularly applicable for time-critical clinical applications. The performance of distortion correction was evaluated in direct comparison with original, uncorrected data using various quantitative and qualitative assessment criteria. The results demonstrate improved functional mapping accuracy without significant degradation of spatial resolution or alternation

of the functional activation distribution. This provides direct insight into the effectiveness of distortion correction for submillimetre fMRI, as demonstrated in this study.

5. Conflict of Interest

The authors declare no competing interests.

6. Author Contributions

S. Y. designed the research; S.Y. developed the proposed MR imaging sequence and the corresponding image reconstruction software; S.Y. performed data acquisition and analysis; S.Y. wrote the draft of the manuscript and revised it; E.G. introduced the geometric distortion using the ANTs software. N.J.S. and S.Y held critical discussions; N.J.S. reviewed and revised the manuscript; N.J.S supported the maintenance and use of the 7T MRI scanner.

7. Funding

E.G. acknowledges support by the Deutsche Forschungsgemeinschaft (DFG) SFB 1280 project A03 and F02 (project number: 316803389). None of the other authors receive any specific grant from funding agencies in the public, commercial, or not-for-profit sectors.

8. Acknowledgements

The authors would like to thank the volunteers for their participation in this work and Claire Rick for English proofreading.

9. Data Availability Statement

The original in vivo data from five subjects can be shared by submitting a request to N. Jon Shah (email: n.j.shah@fz-juelich.de) under a formal data-sharing agreement. The general protection of personal data and privacy policy, declared by the Council of Europe (https://www.coe.int/en/web/portal/personal-data-protection-and-privacy), applies to health-related data (CM/Rec(2019)2). The protection of in vivo data or metadata derived from the original data is further described by the corresponding ethics/internal administrating documents. The sharing is based on the consent of the subject whose data are to be shared; these subjects will be informed beforehand.

References

Aja-Fernandez, S., Martin, D. G., Tristan-Vega, A., & Vegas-Sanchez-Ferrero, G. (2015). Improving GRAPPA reconstruction by frequency discrimination in the ACS lines. Int J Comput Assist Radiol Surg, 10(10), 1699-1710. doi:10.1007/s11548-015-1172-7

Avants, B. B., Tustison, N. J., Song, G., Cook, P. A., Klein, A., & Gee, J. C. (2011). A reproducible evaluation of ANTs similarity metric performance in brain image registration. Neuroimage, 54(3), 2033-2044. doi:10.1016/j.neuroimage.2010.09.025

Balteau, E., Hutton, C., & Weiskopf, N. (2010). Improved shimming for fMRI specifically optimizing the local BOLD sensitivity. Neuroimage, 49(1), 327-336. doi:10.1016/j.neuroimage.2009.08.010

Birn, R. M., Diamond, J. B., Smith, M. A., & Bandettini, P. A. (2006). Separating respiratory-variation-related fluctuations from neuronal-activity-related fluctuations in fMRI. Neuroimage, 31(4), 1536-1548. doi:10.1016/j.neuroimage.2006.02.048

Bright, M. G., & Murphy, K. (2013). Removing motion and physiological artifacts from intrinsic BOLD fluctuations using short echo data. Neuroimage, 64(6), 526-537. doi:10.1016/j.neuroimage.2012.09.043

Chai, Y., Li, L., Wang, Y., Huber, L., Poser, B. A., Duyn, J., & Bandettini, P. A. (2021). Magnetization transfer weighted EPI facilitates cortical depth determination in native fMRI space. Neuroimage, 242, 118455. doi:10.1016/j.neuroimage.2021.118455

Chang, H., & Fitzpatrick, J. M. (1992). A technique for accurate magnetic resonance imaging in the presence of field inhomogeneities. IEEE Trans Med Imaging, 11(3), 319-329. doi:10.1109/42.158935

Chang, Y., Pham, H. A., & Li, Z. (2022). A dual-interpolator method for improving parallel MRI reconstruction. Magn Reson Imaging, 92, 108-119. doi:10.1016/j.mri.2022.06.009

Chen, N. K., & Wyrwicz, A. M. (1999). Correction for EPI distortions using multi-echo gradient-echo imaging. Magn Reson Med, 41(6), 1206-1213. doi:10.1002/(sici)1522-2594(199906)41:6<1206::aid-mrm17>3.0.co;2-l

Chung, J. Y., In, M. H., Oh, S. H., Zaitsev, M., Speck, O., & Cho, Z. H. (2011). An improved PSF mapping method for EPI distortion correction in human brain at ultra high field (7T). MAGMA, 24(3), 179-190. doi:10.1007/s10334-011-0251-1

Deshpande, G., Wang, Y., & Robinson, J. (2022). Resting state fMRI connectivity is sensitive to laminar connectional architecture in the human brain. Brain Inform, 9(1), 2. doi:10.1186/s40708-021-00150-4

Duong, S. T. M., Phung, S. L., Bouzerdoum, A., & Schira, M. M. (2020). An unsupervised deep learning technique for susceptibility artifact correction in reversed phase-encoding EPI images. Magn Reson Imaging, 71, 1-10. doi:10.1016/j.mri.2020.04.004

Dymerska, B., Poser, B. A., Barth, M., Trattnig, S., & Robinson, S. D. (2018). A method for the dynamic correction of B(0)-related distortions in single-echo EPI at 7T. Neuroimage, 168, 321-331. doi:10.1016/j.neuroimage.2016.07.009

Esteban, O., Markiewicz, C. J., Blair, R. W., Moodie, C. A., Isik, A. I., Erramuzpe, A., et al. (2019). fMRIPrep: a robust preprocessing pipeline for functional MRI. Nat Methods, 16(1), 111-116. doi:10.1038/s41592-018-0235-4

Glasser, M. F., Sotiropoulos, S. N., Wilson, J. A., Coalson, T. S., Fischl, B., Andersson, J. L., et al. (2013). The minimal preprocessing pipelines for the Human Connectome Project. Neuroimage, 80, 105-124. doi:10.1016/j.neuroimage.2013.04.127

Griswold, M. A., Jakob, P. M., Heidemann, R. M., Nittka, M., Jellus, V., Wang, J., et al. (2002). Generalized autocalibrating partially parallel acquisitions (GRAPPA). Magn Reson Med, 47(6), 1202-1210. doi:10.1002/mrm.10171

Holland, D., Kuperman, J. M., & Dale, A. M. (2010). Efficient correction of inhomogeneous static magnetic field-induced distortion in Echo Planar Imaging. Neuroimage, 50(1), 175-183. doi:10.1016/j.neuroimage.2009.11.044

Hong, X., To, X. V., Teh, I., Soh, J. R., & Chuang, K. H. (2015). Evaluation of EPI distortion correction methods for quantitative MRI of the brain at high magnetic field. Magn Reson Imaging, 33(9), 1098-1105. doi:10.1016/j.mri.2015.06.010

Huang, P., Correia, M. M., Rua, C., Rodgers, C. T., Henson, R. N., & Carlin, J. D. (2021). Correcting for Superficial Bias in 7T Gradient Echo fMRI. Front Neurosci, 15, 715549. doi:10.3389/fnins.2021.715549

Hutton, C., Bork, A., Josephs, O., Deichmann, R., Ashburner, J., & Turner, R. (2002). Image distortion correction in fMRI: A quantitative evaluation. Neuroimage, 16(1), 217-240. doi:10.1006/nimg.2001.1054

Jezzard, P., & Balaban, R. S. (1995). Correction for geometric distortion in echo planar images from B0 field variations. Magn Reson Med, 34(1), 65-73. doi:10.1002/mrm.1910340111

Jia, K., Zamboni, E., Kemper, V., Rua, C., Goncalves, N. R., Ng, A. K. T., et al. (2020). Recurrent Processing Drives Perceptual Plasticity. Curr Biol, 30(21), 4177-4187 e4174. doi:10.1016/j.cub.2020.08.016

Jia, K., Zamboni, E., Rua, C., Goncalves, N. R., Kemper, V., Ng, A. K. T., et al. (2021). A protocol for ultra-high field laminar fMRI in the human brain. STAR Protoc, 2(2), 100415. doi:10.1016/j.xpro.2021.100415

Kashyap, S., Ivanov, D., Havlicek, M., Poser, B. A., & Uludag, K. (2018). Impact of acquisition and analysis strategies on cortical depth-dependent fMRI. Neuroimage, 168, 332-344. doi:10.1016/j.neuroimage.2017.05.022

Kay, K., Jamison, K. W., Vizioli, L., Zhang, R., Margalit, E., & Ugurbil, K. (2019). A critical assessment of data quality and venous effects in sub-millimeter fMRI. Neuroimage, 189, 847-869. doi:10.1016/j.neuroimage.2019.02.006

Kim, T., Lee, Y., Zhao, T., Hetherington, H. P., & Pan, J. W. (2017). Gradient-echo EPI using a high-degree shim insert coil at 7 T: Implications for BOLD fMRI. Magn Reson Med, 78(5), 1734-1745. doi:10.1002/mrm.26563

Koopmans, P. J., Barth, M., & Norris, D. G. (2010). Layer-specific BOLD activation in human V1. Hum Brain Mapp, 31(9), 1297-1304. doi:10.1002/hbm.20936

Lohmann, G., Stelzer, J., Lacosse, E., Kumar, V. J., Mueller, K., Kuehn, E., et al. (2018). LISA improves statistical analysis for fMRI. Nat Commun, 9(1), 4014. doi:10.1038/s41467-018-06304-z

Mansfield, P. (1977). Multi-Planar Image-Formation Using Nmr Spin Echoes. Journal of Physics C-Solid State Physics, 10(3), L55-L58. doi:Doi 10.1088/0022-3719/10/3/004

Margalit, E., Jamison, K. W., Weiner, K. S., Vizioli, L., Zhang, R. Y., Kay, K. N., & Grill-Spector, K. (2020). Ultra-high-resolution fMRI of Human Ventral Temporal Cortex Reveals Differential Representation of Categories and Domains. J Neurosci, 40(15), 3008-3024. doi:10.1523/JNEUROSCI.2106-19.2020

Margosian, P. (1985). Faster MR. Imaing – Imaging with half the data. Proceedings of the 4th Annual Meeting of SMRM. International Society for Magnetic Resonance in Medicine, p 1024.

Marquardt, I., Schneider, M., Gulban, O. F., Ivanov, D., & Uludag, K. (2018). Cortical depth profiles of luminance contrast responses in human V1 and V2 using 7 T fMRI. Hum Brain Mapp, 39(7), 2812-2827. doi:10.1002/hbm.24042

Menon, R. S. (2002). Postacquisition suppression of large-vessel BOLD signals in high-resolution fMRI. Magn Reson Med, 47(1), 1-9. doi:10.1002/mrm.10041

Montez, D. F., Van, A. N., Miller, R. L., Seider, N. A., Marek, S., Zheng, A., et al. (2023). Using synthetic MR images for distortion correction. Dev Cogn Neurosci, 60, 101234. doi:10.1016/j.dcn.2023.101234

Morgan, P. S., Bowtell, R. W., McIntyre, D. J., & Worthington, B. S. (2004). Correction of spatial distortion in EPI due to inhomogeneous static magnetic fields using the reversed gradient method. J Magn Reson Imaging, 19(4), 499-507. doi:10.1002/jmri.20032

Navarro, K. T., Sanchez, M. J., Engel, S. A., Olman, C. A., & Weldon, K. B. (2021). Depth-dependent functional MRI responses to chromatic and achromatic stimuli throughout V1 and V2. Neuroimage, 226, 117520. doi:10.1016/j.neuroimage.2020.117520

Pais-Roldan, P., Yun, S. D., Palomero-Gallagher, N., & Shah, N. J. (2023). Cortical depth-dependent human fMRI of resting-state networks using EPIK. Front Neurosci, 17, 1151544. doi:10.3389/fnins.2023.1151544

Park, J., Zhang, Q., Jellus, V., Simonetti, O., & Li, D. (2005). Artifact and noise suppression in GRAPPA imaging using improved k-space coil calibration and variable density sampling. Magn Reson Med, 53(1), 186-193. doi:10.1002/mrm.20328

Patzig, F., Mildner, T., Schlumm, T., Muller, R., & Moller, H. E. (2021). Deconvolution-based distortion correction of EPI using analytic single-voxel point-spread functions. Magn Reson Med, 85(5), 2445-2461. doi:10.1002/mrm.28591

Polimeni, J. R., Renvall, V., Zaretskaya, N., & Fischl, B. (2018). Analysis strategies for high-resolution UHF-fMRI data. Neuroimage, 168, 296-320. doi:10.1016/j.neuroimage.2017.04.053

Renvall, V., Witzel, T., Wald, L. L., & Polimeni, J. R. (2016). Automatic cortical surface reconstruction of high-resolution T1 echo planar imaging data. Neuroimage, 134, 338-354. doi:10.1016/j.neuroimage.2016.04.004

Robson, M. D., Gore, J. C., & Constable, R. T. (1997). Measurement of the point spread function in MRI using constant time imaging. Magn Reson Med, 38(5), 733-740. doi:10.1002/mrm.1910380509

Schellekens, W., Bhogal, A. A., Roefs, E. C., Baez-Yanez, M. G., Siero, J. C., & Petridou, N. (2023). The many layers of BOLD. The effect of hypercapnic and hyperoxic stimuli on macro- and micro-vascular compartments quantified by CVR, M, and CBV across cortical depth. J Cereb Blood Flow Metab, 43(3), 419-432. doi:10.1177/0271678X221133972

Shah, N. J., & Zilles, K. (2003). Verfahren zur Untersuchung eines Objekts mittels Erfassung des Ortsfrequenzraumes. DE 000019962845 C2.

Shah, N. J., & Zilles, K. (2004). Imaging process in the spatial frequency space and useful for examining the properties of object. US 6781372 B2.

Sheng, J., Shi, Y., & Zhang, Q. (2021). Improved parallel magnetic resonance imaging reconstruction with multiple variable density sampling. Sci Rep, 11(1), 9005. doi:10.1038/s41598-021-88567-z

Stanley, O. W., Kuurstra, A. B., Klassen, L. M., Menon, R. S., & Gati, J. S. (2021). Effects of phase regression on high-resolution functional MRI of the primary visual cortex. Neuroimage, 227, 117631. doi:10.1016/j.neuroimage.2020.117631

Tustison, N. J., Cook, P. A., Holbrook, A. J., Johnson, H. J., Muschelli, J., Devenyi, G. A., et al. (2021). The ANTsX ecosystem for quantitative biological and medical imaging. Sci Rep, 11(1), 9068. doi:10.1038/s41598-021-87564-6

van der Zwaag, W., Buur, P. F., Fracasso, A., van Doesum, T., Uludag, K., Versluis, M. J., & Marques, J. P. (2018). Distortion-matched T(1) maps and unbiased T(1)-weighted images as anatomical reference for high-resolution fMRI. Neuroimage, 176, 41-55. doi:10.1016/j.neuroimage.2018.04.026

Wang, J., Nasr, S., Roe, A. W., & Polimeni, J. R. (2022). Critical factors in achieving fine-scale functional MRI: Removing sources of inadvertent spatial smoothing. Hum Brain Mapp, 43(11), 3311-3331. doi:10.1002/hbm.25867

Wang, X., Wang, H., & Zhou, J. (2014). Improve GRAPPA with cross-sampled ACS lines and nonlinear kernel model. Biomed Mater Eng, 24(1), 1101-1108. doi:10.3233/BME-130909

Yip, C. Y., Fessler, J. A., & Noll, D. C. (2006). Advanced three-dimensional tailored RF pulse for signal recovery in T2*-weighted functional magnetic resonance imaging. Magn Reson Med, 56(5), 1050-1059. doi:10.1002/mrm.21048

Yun, S. D., Kuppers, F., & Shah, N. J. (2023a). Submillimeter fMRI Acquisition Techniques for Detection of Laminar and Columnar Level Brain Activation. J Magn Reson Imaging. doi:10.1002/jmri.28911

Yun, S. D., Pais-Roldan, P., Palomero-Gallagher, N., & Shah, N. J. (2022). Mapping of whole-cerebrum resting-state networks using ultra-high resolution acquisition protocols. Hum Brain Mapp, 43(11), 3386-3403. doi:10.1002/hbm.25855

Yun, S. D., Reske, M., Vahedipour, K., Warbrick, T., & Shah, N. J. (2013). Parallel imaging acceleration of EPIK for reduced image distortions in fMRI. Neuroimage, 73, 135-143. doi:10.1016/j.neuroimage.2013.01.070

Yun, S. D., & Shah, N. J. (2017). Whole-brain high in-plane resolution fMRI using accelerated EPIK for enhanced characterisation of functional areas at 3T. PLoS One, 12(9), e0184759. doi:10.1371/journal.pone.0184759

Yun, S. D., & Shah, N. J. (2023b). A simultaneous measurement of opposite-phase-encoding EPI in a single fMRI session for the reduction of acquisition time and SAR at 7T. Proceedings of the 32nd Annual Meeting of ISMRM. International Society for Magnetic Resonance in Medicine, Toronto, Abstract 1161.

Yun, S. D., Weidner, R., Weiss, P. H., & Shah, N. J. (2019). Evaluating the Utility of EPIK in a Finger Tapping fMRI Experiment using BOLD Detection and Effective Connectivity. Sci Rep, 9(1), 10978. doi:10.1038/s41598-019-47341-y

Zaitsev, M., Hennig, J., & Speck, O. (2004). Point spread function mapping with parallel imaging techniques and high acceleration factors: fast, robust, and flexible method for echo-planar imaging distortion correction. Magn Reson Med, 52(5), 1156-1166. doi:10.1002/mrm.20261

Zaitsev, M., Zilles, K., & Shah, N. J. (2001). Shared k-space echo planar imaging with keyhole. Magn Reson Med, 45(1), 109-117. doi:10.1002/1522-2594(200101)45:1<109::aid-mrm1015>3.0.co;2-x

Zeng, H., & Constable, R. T. (2002). Image distortion correction in EPI: comparison of field mapping with point spread function mapping. Magn Reson Med, 48(1), 137-146. doi:10.1002/mrm.10200

Zheng, H., Zhao, T., Qian, Y., Schirda, C., Ibrahim, T. S., & Boada, F. E. (2013). Multi-slice parallel transmission three-dimensional tailored RF (PTX 3DTRF) pulse design for signal recovery in ultra high field functional MRI. J Magn Reson, 228, 37-44. doi:10.1016/j.jmr.2012.12.021

Figures

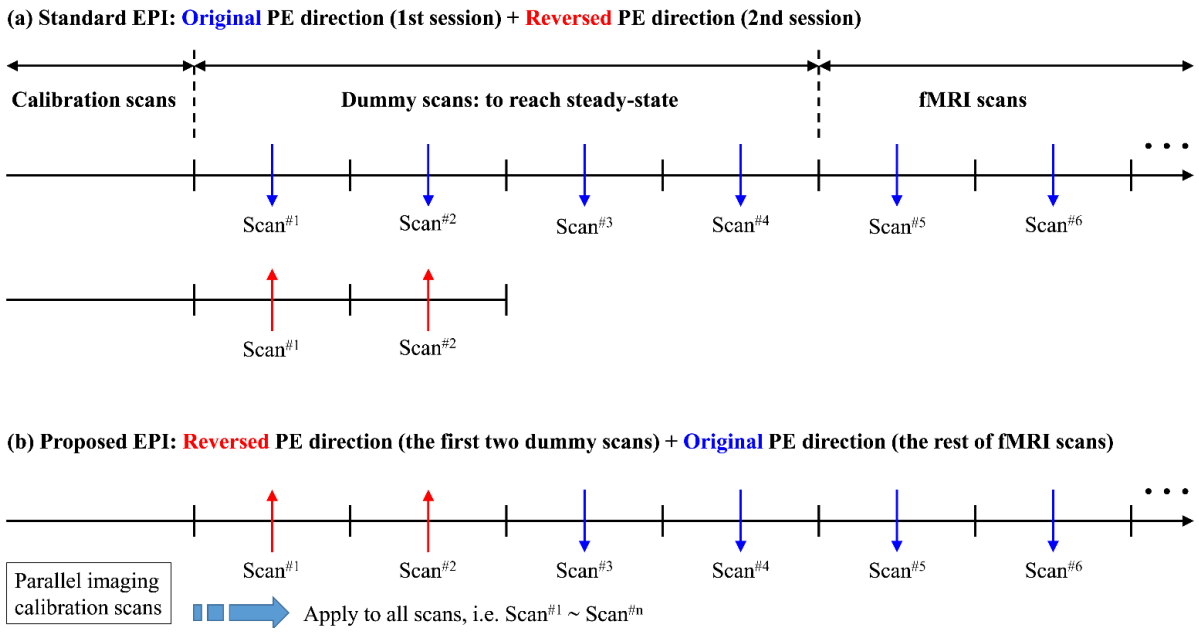

Figure 1. Schematic diagram of an fMRI acquisition sequence. (**a**) Standard EPI and (**b**) proposed EPI. In the standard scheme, the reversed PE data are acquired in a separate session, requiring repeated measurements for the calibration scan. In contrast, the proposed scheme acquires the reversed PE data during the same session at the dummy stage, using the same calibration scan for image reconstruction. The blue and red arrows denote the original and reversed PE directions, respectively. In this work, the number of dummy and reversed PE scans was configured to four and two, as illustrated in the figure.

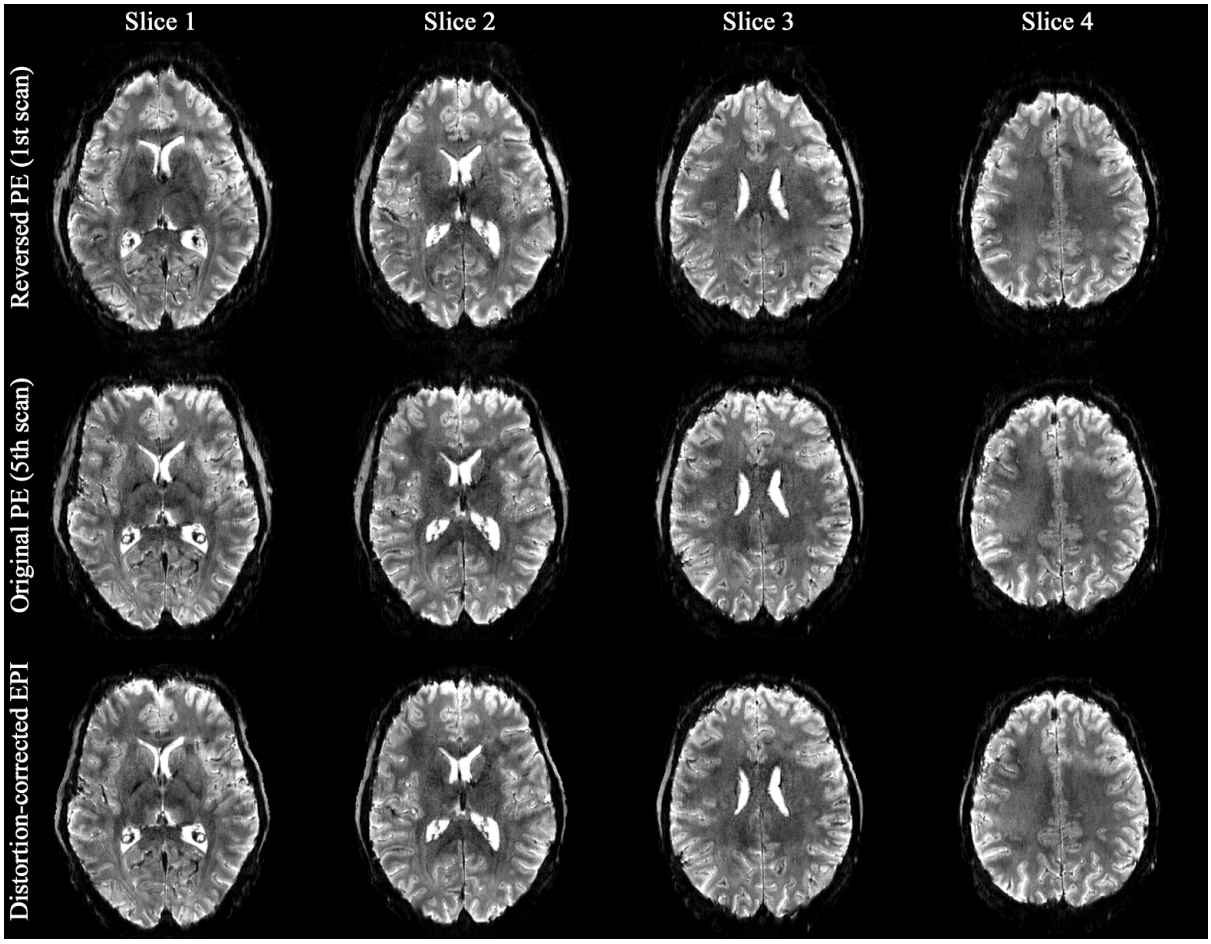

Figure 2. Reconstructed images at four representative slice locations. The first and second rows display images obtained from the reversed and original PE directions. The last row shows the corresponding distortion-corrected results, revealing no significant visible loss of spatial resolution.

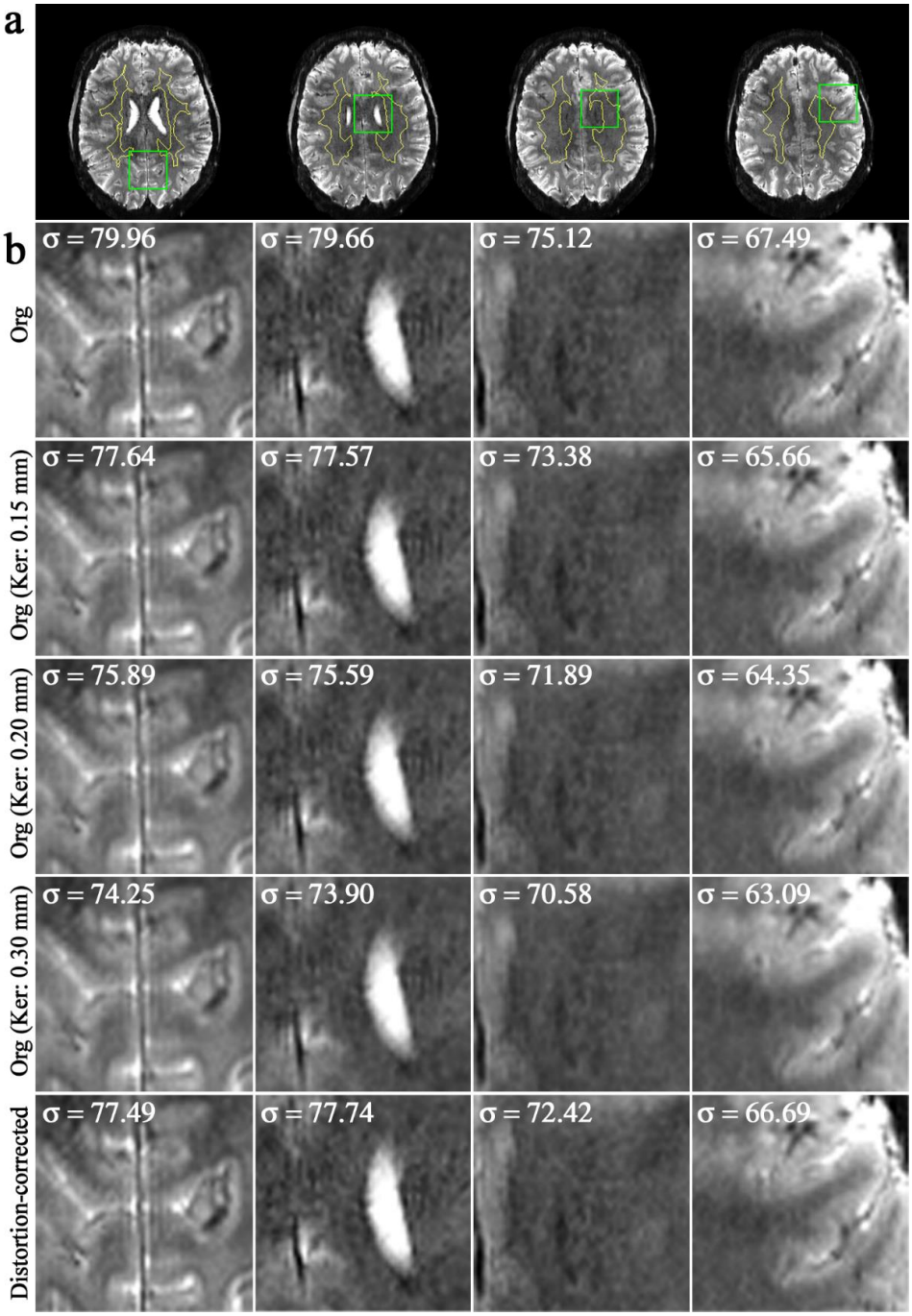

Figure 3. Results of spatial resolution assessments. (**a**) Original EPI images at four selected slice locations where the quantitative assessment of spatial resolution was performed. (**b**) From top to bottom, enlarged depictions of the rectangular ROIs marked in green are shown for the following: original EPI, original EPI smoothed with a Gaussian kernel width of 0.15, 0.20 and 0.30, and distortion-corrected EPI. For each case, the SD computed for the yellow ROI is also shown alongside. The results of visual inspection and SD values verify that the loss of spatial resolution is not significant in the distortion-corrected images.

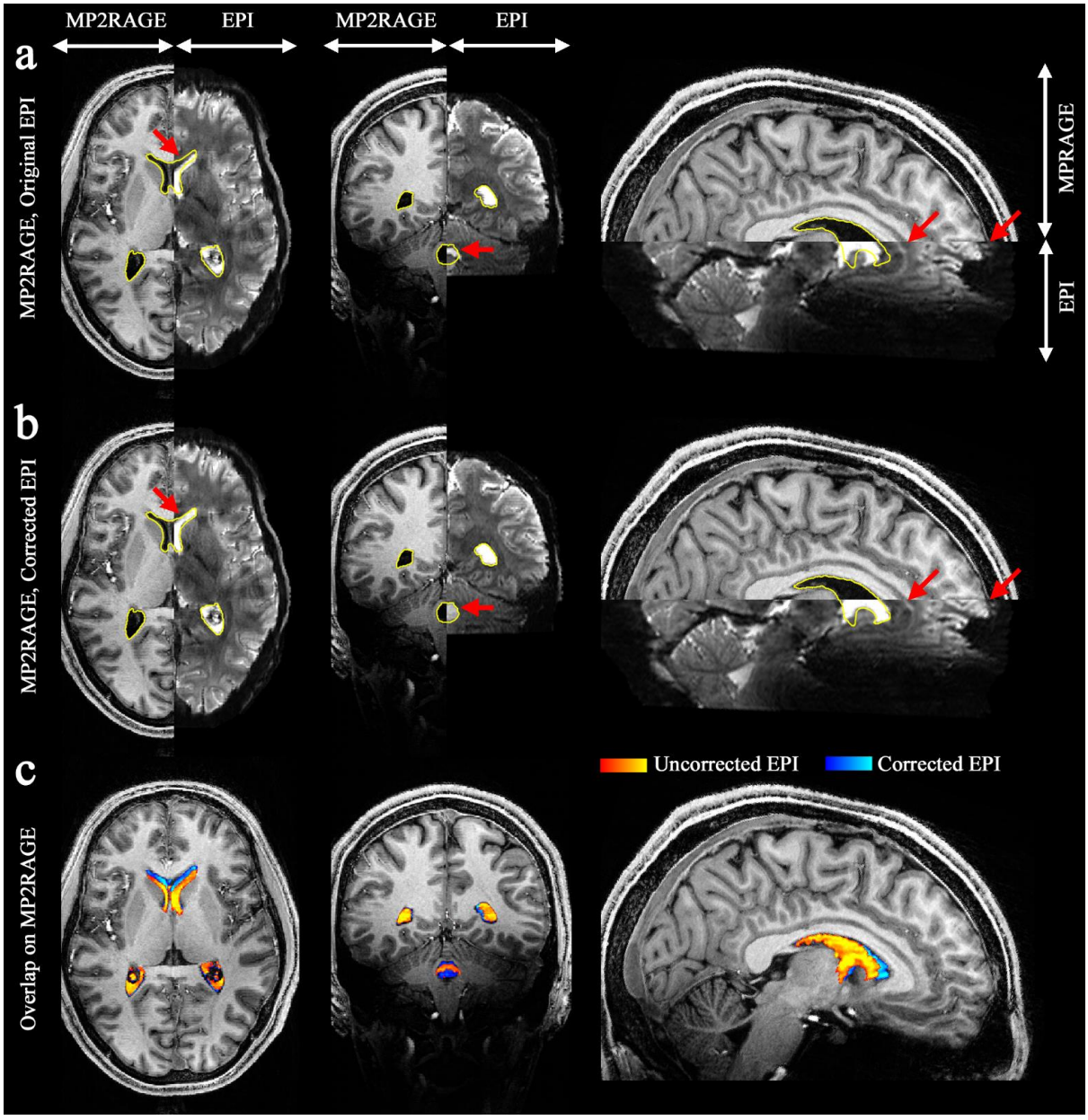

Figure 4. Results of co-registration to the anatomical scan (MP2RAGE). (**a**) Original EPI, (**b**) distortion-corrected EPI and (**c**) both results overlaid onto the MP2RAGE. In image panels a and b, the EPI and MP2RAGE scans are displayed alongside, each depicting the counterpart of the brain. The results from distortion-corrected EPI show improved alignment with the MP2RAGE scan, particularly around the regions marked by yellow boundaries (i.e. lateral and fourth ventricles) and red arrows; the boundary between the cingulate gyrus and corpus callosum is also shown to be well aligned. The overlapped depiction in image panel c further confirms the improved co-registration, where the ventricle signals are represented in red-yellow for the original EPI and blue-light blue for the corrected EPI.

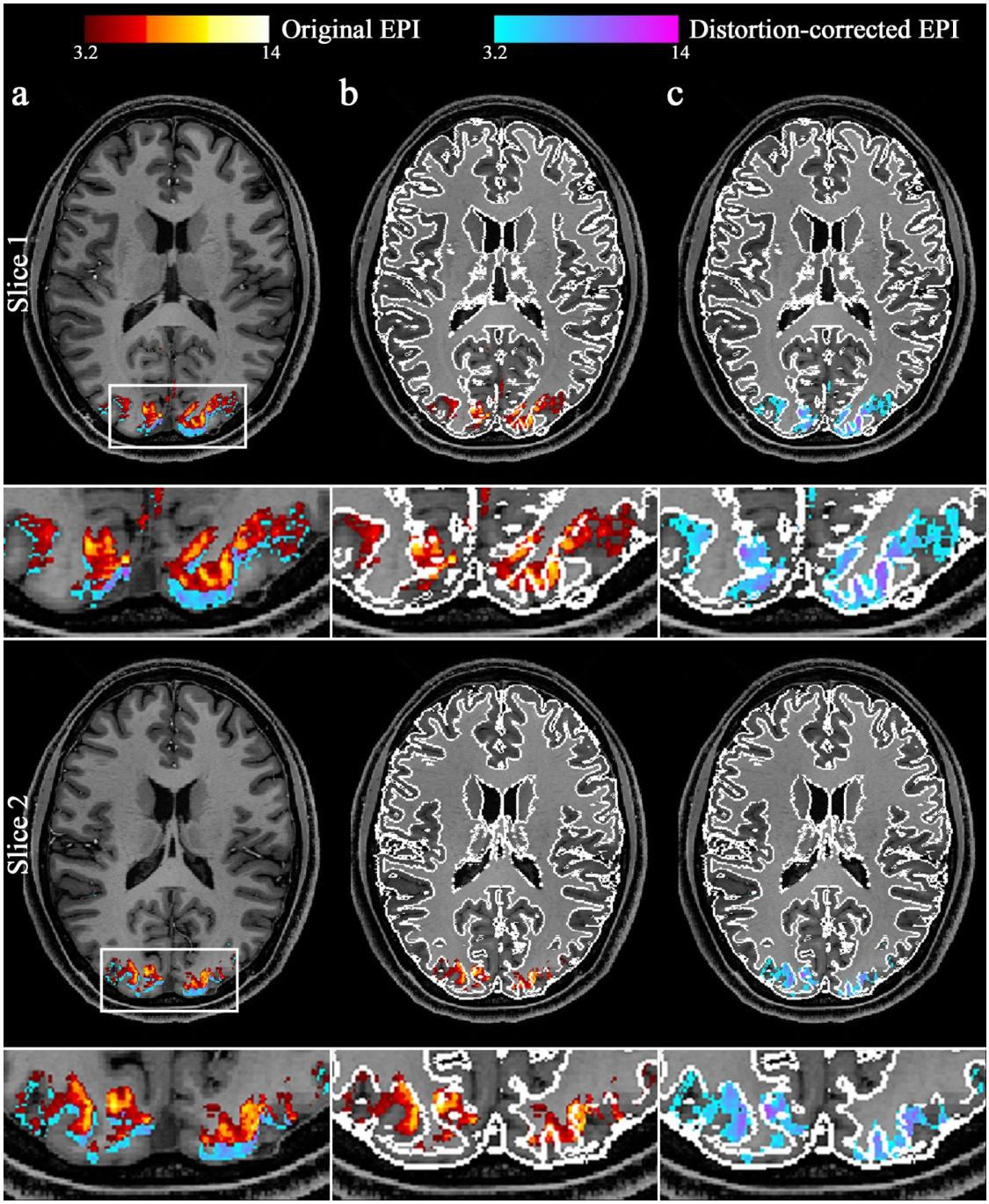

Figure 5. Results of first-level analysis for visual fMRI (uncorrected $p < 0.001$). (**a**) The original (denoted in red-white) and distortion-corrected (denoted in cyan-magenta) results are overlaid on the co-registered MP2RAGE scan, revealing substantial differences in the localisation of activated voxels at the selected slice locations. A separate representation of the (**b**) original and (**c**) distortion-corrected results with the GM contour (denoted in white) further demonstrates that the activated voxels are more precisely localised along the cortical ribbon in the distortion-corrected case; see the enlarged depiction of the selected ROIs.

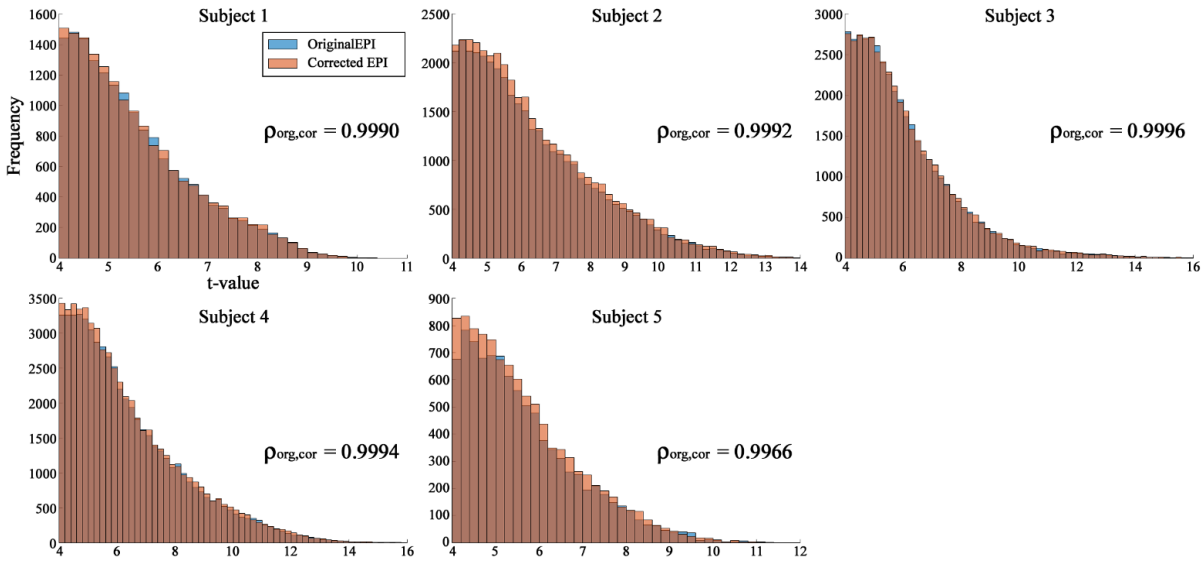

Figure 6. Analysis of histogram distribution from five subjects. For each subject, the histogram distribution of t-values obtained from the original (denoted in blue) and distortion-corrected (denoted in orange) fMRI data sets are depicted on the same plot, with the computed Pearson correlation coefficient. The histogram distribution and correlation values ($\rho > 0.99$ for all subjects) show a high degree of similarity, implying that distortion correction did not significantly impact the distribution of functional activation.

Tables

Table 1. Acquisition time (s) and time-averaged power (W) required for the parallel imaging calibration scan. The results are shown for a range of ACS lines (24, 48, and 72) and TR (10, 15, and 20 ms), when a SPGR sequence is implemented with a flip angle of 15°. For each case, the time and power required for the entire measurement are also provided, along with the proportion occupied by those for the parallel imaging calibration scan (see the percentages in the parentheses).

ACS lines	**TR (ms)**		
	10	**15**	**20**
24	39.78 / 421.29 s (9.44 %) 2.51 / 5.45 W (46.10 %)	59.67 / 441.18 s (13.53 %) 2.01 / 5.21 W (38.50 %)	79.56 / 461.07 s (17.26 %) 1.67 / 4.98 W (33.46 %)
48	67.86 / 449.37 s (15.10 %) 1.93 / 5.13 W (37.62 %)	101.79 / 483.30 s(21.06 %) 1.46 / 4.77 W (30.67 %)	135.72 / 517.23 s(26.24 %) 1.18 / 4.46 W (26.43 %)
72	95.94 / 477.45 s (20.09 %) 1.59 / 4.85 W (32.81 %)	143.91 / 525.42 s(27.39 %) 1.17 / 4.41 W (26.61 %)	191.88 / 573.39 s(33.46 %) 0.93 / 4.04 W (22.99 %)

Table 2. The ratio of activated voxels located in the GM and in other regions (i.e. non-GM). The results from distortion-corrected EPI show substantial increases in the ratio of GM-located activated voxels (88.58 ± 2.51%) when compared to those from original, uncorrected EPI (80.25 ± 1.69%).

Subject	**Uncorrected EPI**		**Corrected EPI**	
	GM (%)	**Non-GM (%)**	**GM (%)**	**Non-GM (%)**
1	78.96	21.04	88.86	11.14
2	78.50	21.50	86.43	13.57
3	82.78	17.22	89.09	10.91
4	80.73	19.27	86.16	13.84
5	80.30	19.70	92.38	7.62
mean ± SD	80.25 ± 1.69	19.75 ± 1.69	88.58 ± 2.51	11.42 ± 2.51